

Hydrogen evolution reaction on Co-Ni core-shell nanoclusters in different sizes: A DFT investigation from geometric structures to electronic structures

Hengyue Xu*

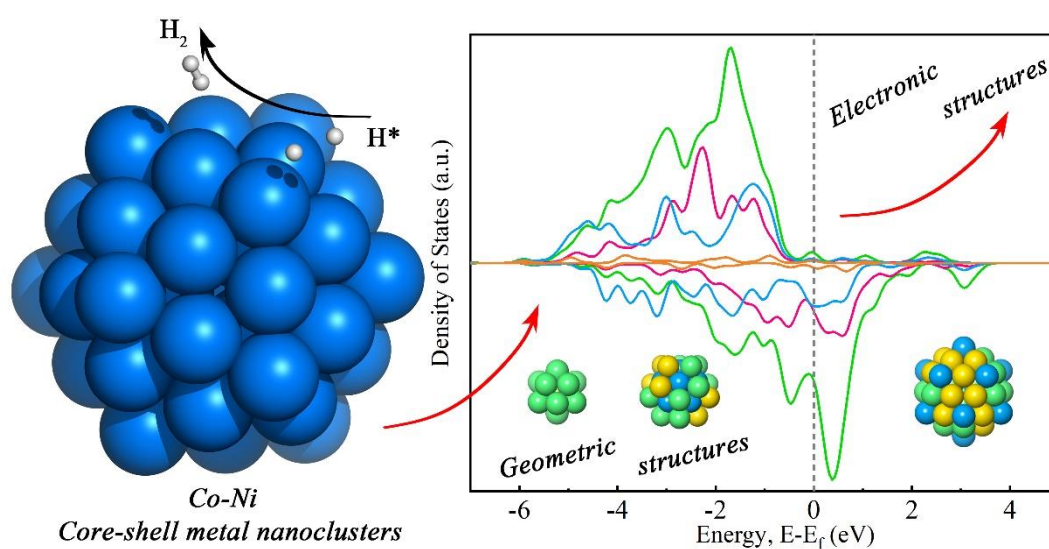
*State Key Laboratory of Chemical Oncogenomics, Tsinghua Shenzhen International Graduate School, Tsinghua University, Shenzhen, People's Republic of China.

Corresponding author:

Hengyue Xu, Email: xuhy21@mails.tsinghua.edu.cn

ORCID iD <https://orcid.org/0000-0003-4438-9647>

Graphical abstract



Abstract

Nanoclusters have broad prospects in the application of hydrogen evolution reaction (HER) electrocatalysis. Its high specific surface area, surface geometry effect, electronic properties, and quantum size effect often make the nanoclusters have higher activity than ordinary electrocatalytic materials. However, it is still challenging to design and regulate nanoclusters and make them have better HER performance. In this work, through first-principles calculation from geometric structures to electronic structures, we try to understand the basic physical and chemical properties and HER performance of nanoclusters composed of transition metals Co and Ni. We optimize the electronic structure and promote effective charge transfer by adjusting the size of nanoclusters and constructing core-shell alloying. First-principles studies reveal that the geometric size and electronic structures of Co-Ni nanoclusters can significantly affect the performance of the hydrogen evolution reaction. We found that Co@Ni₁₂ ($|\Delta G_{H^*}|=0.01\text{eV}$) shows the best HER performance. The Gibbs free energy of hydrogen adsorption of Co-Ni nanoclusters is positively related to the size of the clusters, and the ΔG_{H^*} can be adjusted within a certain range by changing the electronic structures of the clusters. Our research helps to understand and design high-efficiency nanocluster electrocatalysts, paving the way for the rational design and synthesis of advanced electrocatalysts for HER.

Keywords: Co–Ni core-shell nanoclusters, Hydrogen evolution reaction (HER), Charge transfer, Electronic and magnetic properties, Catalytic activity, DFT calculation

INTRODUCTION

Since human society entered the industrial revolution, fossil fuels have long dominated the social economy and have become the material basis for human survival and development. However, this dependence is not sustainable. The consumption of a large number of fossil fuels not only leads to an imminent energy crisis, but excessive carbon emissions can also cause serious environmental problems. As a green, efficient, and

sustainable energy source, hydrogen energy, with its high-power density and zero emissions, is expected to replace fossil fuels and become the "green engine" for the operation of human society in the future.

71% of the earth's surface is the ocean, which stores huge hydrogen energy. The key to obtaining hydrogen energy from aqueous solutions depends on developing high-efficiency electrocatalysts for oxygen evolution reaction (OER) and hydrogen evolution reaction (HER). As we all know, Pt-based materials have high exchange current density and state-of-the-art electrocatalytic performance for hydrogen evolution reactions (HER)^{1, 2}. Unfortunately, the high cost and scarce reserves have become a stumbling block for the large-scale application of Pt-based materials. Therefore, it remains a critical task to explore and develop new electrode materials with abundant reserves on the earth to replace precious metal electrocatalysts.

From the perspective of electronic structure, in addition to precious metals like Pt, the transition metals Co and Ni, which are abundant in reserves, also have the potential to serve as hydrogen evolution reactions (HER) catalysts. Co and Ni are 3d metals, spin-polarized; the spin-up and spin-down d-bands are shifted with respect to each other. It is relatively easy to form Co-H and Ni-H bonds for Co, Ni, and its binary alloy catalysts³. At present, alloy materials composed of Co and Ni have been proven to have high-efficiency HER performance and are expected to replace expensive and scarce Pt-based materials^{4, 5}. In recent years, nanoscience and nanotechnology have developed rapidly. Compared with traditional bulk electrocatalysts, the nano-sized Co and Ni alloy structure not only enhances the HER activity in the synergistic effect⁶ but its high specific surface area, surface geometric effect, electronic properties, and quantum size effect also make it have better HER performance⁷.

Although the current research on Co-Ni nanomaterials has been extensive, there is still a lack of understanding of Co-Ni nanostructures at the atomic level. The relationship between the microscopic geometric structure, electronic structure, and electrocatalytic performance of Co-Ni nanoclusters or nanoparticles is still unclear. Therefore, it is still

challenging to design Co-Ni nanoscale structures with good performance of HER. In view of the above problems, in order to further understand and design Co-Ni nanoclusters suitable for HER reaction, the geometric structure, thermodynamic stability, charge transfer, chemical activity, electronic, and magnetic properties of 13-33- and 55-atoms Co, Ni monometallic nanoclusters and Co-Ni bimetallic core-shell nanoclusters (BCSNCs) were comparatively investigated using density functional theory (DFT) calculations. Furthermore, we also evaluated the performance of these nanoclusters with different geometric structures, sizes, and compositions on the HER reaction. Finally, we found that Co@Ni₁₂ ($|\Delta G_{H^*}|=0.01\text{eV}$) shows the best HER performance. The size, composition, and electronic structure of the Co-Ni nanoclusters are potentially related to the ΔG_{H^*} of the hydrogen adsorption. The results will help provide a certain theoretical basis and guidance for the controllable synthesis of Co-Ni nanoclusters and the rational design of advanced HER electrocatalysts.

COMPUTATIONAL DETAILS

All spin-polarized DFT calculations were performed with the Vienna Ab initio simulation package (VASP⁸). The exchange-correlation function was handled using the generalized gradient approximation (GGA) formulated by the Perdew-Burke-Ernzerhof (PBE)⁹. The interaction between the atomic core and electrons was described by the projector augmented wave method^{10,11}. The plane-wave basis set energy cutoff was set to 400 eV. A $1 \times 1 \times 1$ k-point mesh for the reciprocal space integration was employed for all the calculations with a discrete character. The periodic boundary conditions were implemented with at least 10 Å vacuum to preclude the interaction between a cluster and its image. The simulation boxes were $15 \times 15 \times 15$ for 13-atoms and $20 \times 20 \times 20$ Å for 33, 55-atoms configurations, respectively. The spin-polarized calculations were performed starting from default values of NIONS*1.0 as the initial magnetic moment for each atom in the VASP code. All structures with a dynamic magnetic moment were fully relaxed to optimize without any restriction until their total energies were converged to $<10^{-6}$ eV, and the average residual forces were <0.01 eV/Å¹². The global

transferred charge was calculated by the atomic Bader charge analysis^{13, 14}.

RESULTS AND DISCUSSION

Co-Ni Core-shell alloyed clusters show similar geometries

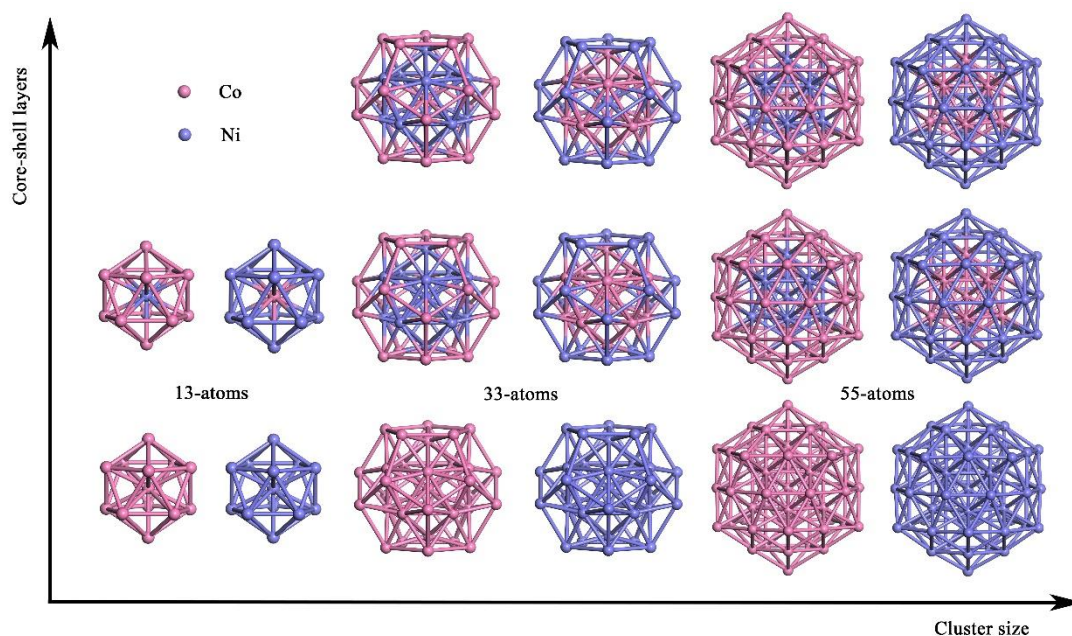


Figure 1. The geometry structures of 13, 33, and 55-atoms monometallic and bimetallic Co-Ni core-shell nanoclusters. Magenta and violet spheres represent Co and Ni atoms, respectively.

With spin-polarized DFT calculations, the 13, 33, and 55-atoms monometallic and bimetallic Co-Ni core-shell nanoclusters are displayed in two dimensions of cluster size and the number of core-shell layers, corresponding to the lowest energy. (Figure 1) From the dimension of cluster size, the 13-atoms clusters have an icosahedral geometry structure. The 33-atoms clusters are constructed by adsorbing 20 Co or Ni atoms on the (111)-shaped surfaces of the 13-atoms clusters, and they show a dodecahedral geometry. Unlike the 33-atoms cluster, the 55-atoms cluster is constructed by adsorbing 42 Co or Ni atoms on 12 vertices and 30 bonds on the 13-atoms cluster, respectively. It shows an icosahedral geometry similar to the 13-atoms cluster. From the dimension of core-shell layers, 13, 33, and 55-atoms core-shell clusters are constructed by replacing the cluster layers with different elements. Detailed geometric structure analysis data can be

found in the supporting information. The geometric structure analysis shows that the surface bond length of the 33-atoms Co-Ni clusters is significantly longer than 13 and 55 atoms. Core-shell alloying of clusters can change the bond length of clusters to a certain extent, but their overall structure is not very different.

Ni-surface clusters have higher relative stability than Co-surface

In order to compare the relative stability of these core-shell nanoclusters, the excess energy (E_{exc}) of $A_m@B_n$, $B@A_m@B_{n-1}$ are defined as follows:^{15, 16}

$$E_{exc} = E_{A_m@B_n/B@A_{m-1}@B_n} - \frac{m}{m+n} E_{A_{(m+n)}} - \frac{n}{m+n} E_{B_{(m+n)}}$$

$E_{A_m@B_n/B@A_m@B_{n-1}}$, $E_{A_{(m+n)}}$, $E_{B_{(m+n)}}$ are the symbols in this formula meaning total energy of monometallic and bimetallic core-shell nanoclusters, A and B with the same size ($m+n$ atoms) and geometry structures, respectively. In this study, the excess energy (E_{exc}) of the monometallic nanoclusters is set to zero as a reference for the corresponding bimetallic nanoclusters benchmark. The negative value of (E_{exc}) usually indicates (E_{exc}) in general the energetically favorable configuration.

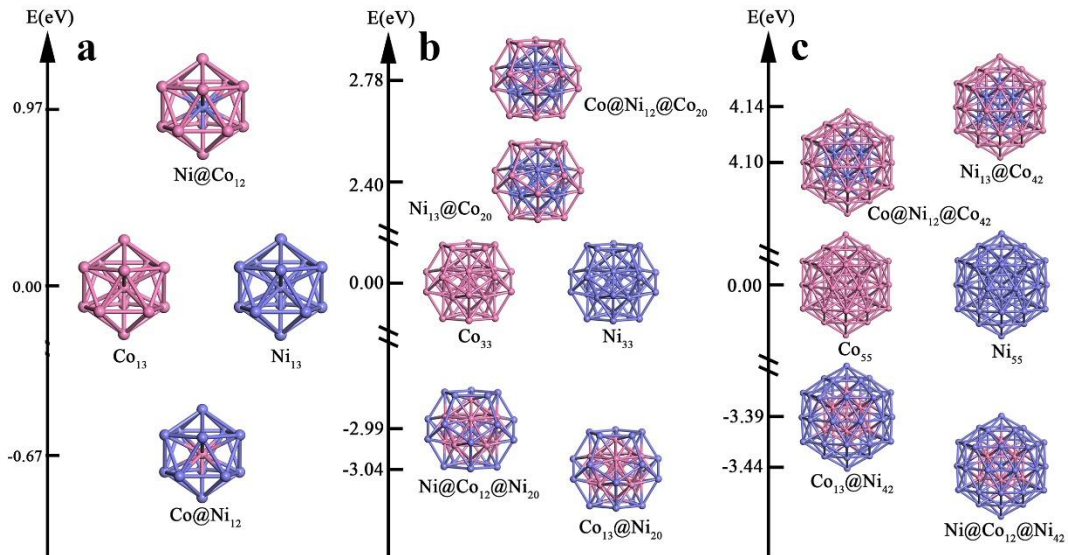


Figure 2. The excess energies of a 13-atoms b 33-atoms and c 55-atoms Co, Ni nanoclusters. Magenta and violet spheres represent Co and Ni atoms, respectively.

With the excess energies displayed in Figure 2, we can easily know that the relative

stabilities of these Co-Ni nanoclusters follow the order Ni@Co₁₂ (0.97 eV) < Co₁₃/Ni₁₃ (0.00 eV) < Co@Ni₁₂ (-0.67 eV) (Fig. 2a). Co@Ni₁₂@Co₂₀ (2.78 eV) < Ni₁₃@Co₂₀ (2.40 eV) < Co₅₅/Ni₅₅ (0.00 eV) < Ni@Co₁₃@Ni₂₀ (-2.99 eV) < Co₁₃@Ni₂₀ (-3.04 eV) (Fig. 2b). Ni₁₃@Co₄₂ (4.14 eV) < Co@Ni₁₂@Co₄₂ (4.10 eV) < Co₅₅/Ni₅₅ (0.00 eV) < Co₁₃@Ni₄₂ (-3.39 eV) < Ni@Co₁₂@Ni₄₂ (-3.44 eV) (Fig. 2c). Research shows that the Co@Ni₁₂ (-0.67 eV) cluster, which with a Ni surface-shell, possessing the lowest excess energies below than the corresponding monometallic Co₁₃/Ni₁₃ (0.00 eV), however the Ni@Co₁₂ (0.97 eV) cluster, which with a Co surface-shell, have the highest excess energies than the corresponding monometallic Co₁₃/Ni₁₃ (0.00 eV). Analogously, the 33-atoms nanoclusters system in Figure 2b displays the Ni@Co₁₃@Ni₂₀ (-2.99 eV) and Co₁₃@Ni₂₀ (-3.04 eV) nanoclusters, which with a Ni surface-shell, below than the corresponding monometallic Co₃₃/Ni₃₃ (0.00 eV) and Co@Ni₁₂@Co₂₀ (2.78 eV), Ni₁₃@Co₂₀ (2.40 eV) clusters, which with a Co surface-shell, are above it. However, it is interesting that two-layer Co₁₃@Ni₂₀ has lower excess energy than three-layer Ni@Co₁₃@Ni₂₀ by only 0.05 eV, while three-layer Co@Ni₁₂@Co₂₀ has higher excess energy than two-layer Ni₁₃@Co₂₀ by 0.38 eV. More interestingly, it is roughly the same in the 55-atoms nanoclusters system in Figure 2c, but somewhat different because three-layer Ni@Co₁₂@Ni₄₂ has lower excess energy than two-layer Co₁₃@Ni₄₂ by only 0.05 eV, while two-layer Ni₁₃@Co₂₀ has higher excess energy than three-layer Co@Ni₁₂@Co₄₂ by only 0.04 eV. As a result, it is contrary to the stability tendency in the 33-atoms nanoclusters system (two-layer > three-layer) and 55-atoms nanoclusters system (three-layer > two-layer). The total energy, excess energy, magnetic moment have displayed in Table I.

Table 1 Calculated results of total, excess, and segregation energies and magnetic moment of monometallic and bimetallic Co-Ni core-shell nanoclusters.

Nanoparticle	E_{total} (eV)	E_{exc} (eV)	Magnetic moment (μB)
Co ₁₃	-67.09536517	0.00	21.77
Ni ₁₃	-49.92385286	0.00	8.00
Ni@Co ₁₂	-64.80702514	0.97	20.64
Co@Ni ₁₂	-51.91461042	-0.67	9.05
Co ₃₃	-190.2894001	0.00	60.89
Ni ₃₃	-140.1012015	0.00	28.34
Ni ₁₃ @Co ₂₀	-168.1124673	2.40	51.77
Co ₁₃ @Ni ₂₀	-162.9074197	-3.04	40.69
Co@Ni ₁₂ @Co ₂₀	-169.2618989	2.78	51.23
Ni@Co ₁₂ @Ni ₂₀	-161.3447238	-2.99	39.69
Co ₅₅	-331.8413366	0.00	104.45
Ni ₅₅	-249.8686900	0.00	38.89
Ni ₁₃ @Co ₄₂	-308.3245820	4.14	88.51
Co ₁₃ @Ni ₄₂	-272.6302020	-3.39	52.43
Co@Ni ₁₂ @Co ₄₂	-309.8582922	4.10	91.26
Ni@Co ₁₂ @Ni ₄₂	-271.1891057	-3.44	51.62

The bimetallic Co-Ni core-shell nanoclusters have a more complex charge distribution

Under the situation of bimetallic core-shell, the nanoclusters with the hetero-nuclear metal atoms may further be enhanced or inhibited the charge transfer among the inner and surface atoms due to the different electronic structures and electronegativity. In order to further study the charge density, which is affected by the switch of the inner-core and surface-shell atoms, of the bimetallic Co-Ni core-shell nanoclusters, Bader charge analysis, and the results are displayed in Figure 3. In this figure, the negative Bader charge corresponds to net charge accumulation, while the positive Bader charge indicates net charge depletion on the core-shell atoms. Detailed Bader charge data can be found in the supporting information Table S3.

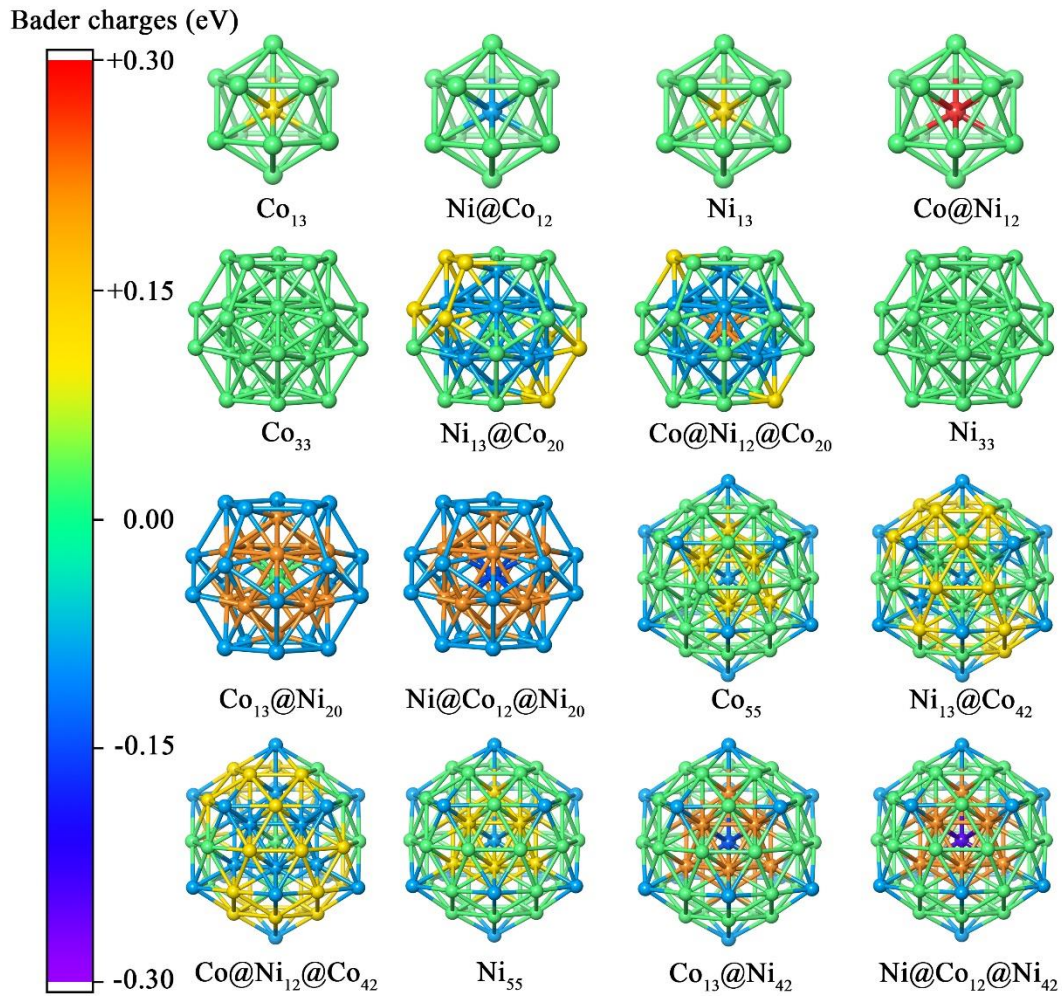


Figure 3. The Bader charges analysis of the 13, 33, and 55-atoms monometallic and bimetallic Co-Ni core-shell nanoclusters.

As known to all, the electron tends to transfer from inner atoms to surface atoms due to the surface effect in monometallic nanoclusters generally. For 13-atoms monometallic nanoclusters, the net charge transfer from one core atom to 12 surface-shell atoms is 0.10 electron (e) for Co_{13} and $0.09e$ for Ni_{13} . For 33-atoms monometallic nanoclusters, the net charge transfer from 13 inner atoms to 20 surface-shell atoms is 0.49 electron (e) for Co_{33} and $0.50e$ for Ni_{33} . The charge distributions of Co_{33} and Ni_{33} are $+0.02$ $+0.47$ and $-0.49e$ and $+0.03$ $+0.47$ and $-0.50e$ for the core, middle-shell, and surface-shell atoms, respectively. Interestingly, the charge distributions of Co_{55} are -0.13 , $+0.70$, and $-0.57e$ for the core, middle-shell, and surface-shell atoms, respectively. Similarly, the charge distributions of Ni_{55} are -0.14 , $+0.82$, and $-0.68e$ for the core, middle-shell,

and surface-shell atoms, respectively.

The electron transfer from Co to Ni in the heterojunction of the bimetallic Co-Ni core-shell nanoclusters would be further enhanced due to the difference of electronegativity between Co (1.88) and Ni (1.91). As the Bader charge analysis displayed in Figure 3, the charge always transfers from Co atoms to Ni atoms. Besides, charge transfer would also be enhanced from Co to Ni due to the synergistic effects of the surface when Ni locates at the surface and Co locates at the inner-shell. For the 13-atoms bimetallic nanoclusters Co@Ni_{12} , the net charge of $0.26e$ is transferred from one Co core atom to 12 surface-shell Ni atoms, leading to a more negative surface-shell than that of Ni_{13} by $0.17e$. Surprisingly, the charge transfer has been dramatically enhanced in the bimetallic nanoclusters $\text{Co}_{13}\text{@Ni}_{20}$ and $\text{Co}_{13}\text{@Ni}_{42}$, resulting in a much more negative surface-shell than that of Ni_{33} and Ni_{55} by $1.51e$ and $1.15e$, respectively. The net charges of $2.01e$ and $1.83e$ are transferred from 13 Co inner atoms to Ni surface in $\text{Co}_{13}\text{@Ni}_{20}$ and $\text{Co}_{13}\text{@Ni}_{42}$. An interesting phenomenon appears in $\text{Co}_{13}\text{@Ni}_{42}$ that the net charges of $0.20e$ are transferred from the Co middle-shell atoms to the core atom Co. Three-shell bimetallic nanoclusters $\text{Ni@Co}_{12}\text{@Ni}_{20}$ and $\text{Ni@Co}_{12}\text{@Ni}_{42}$, modeled from $\text{Co}_{13}\text{@Ni}_{20}$ and $\text{Co}_{13}\text{@Ni}_{42}$ by switching the one Co core-atom with Ni atom, the net charge of 0.16 and $2.03e$ is transferred from 12 Co middle-shell atoms to one core and 20 Ni surface atoms, respectively in $\text{Co}_{13}\text{@Ni}_{20}$, and similarly, the net charge of 0.32 and $1.87e$ is transferred from 12 Co middle-shell atoms to one core and 42 Ni surface atoms, respectively in $\text{Co}_{13}\text{@Ni}_{42}$.

The charge transfer from Co to Ni would be inhibited due to the mutually offset of the surface and electronegativity effects. For 13-atoms Ni@Co_{12} , the net charge of $0.09e$ is transferred from 12 Co surface atoms to the Ni core atom, leading to a more positive surface-shell than that of Co_{13} by $0.19e$. For the bimetallic nanoclusters $\text{Ni}_{13}\text{@Co}_{20}$ and $\text{Ni}_{13}\text{@Co}_{42}$, the net charges of $0.99e$ and $0.66e$ are transferred from Co surface-shell atoms to 13 Ni inner atoms, respectively. For the bimetallic nanoclusters $\text{Co@Ni}_{12}\text{@Co}_{20}$, the net charges of 0.16 and $0.92e$ are transferred from the one core

and 20 surface Co atoms to 12 Ni middle-shell atoms, respectively, and similar with the $\text{Co@Ni}_{12}\text{@Co}_{42}$, the net charges of 0.03 and $0.67e$ are transferred from the one core and 20 surface Co atoms to 12 Ni middle-shell atoms, respectively.

Ni-surface clusters have higher chemical activity than Co-surface

With the different charge transfer, the different chemical activities of bimetallic Co-Ni core-shell nanoclusters may be endowed, which still needs a further understanding of the charge-transfer-induced chemical activity. The density of states (DOS) onto the d-band of these monometallic and bimetallic Co-Ni core-shell nanoclusters was calculated and displayed in Figure 4. The Ni@Co bimetallic nanoclusters with the Co surface shell, the d-band states shift away from the Fermi level compared to that of the Co monometallic nanoclusters. Figures 4(a)–4(h) show that the d-band centers shift from -1.48 (Co_{13}) to -1.53 eV (Ni@Co_{12}) for 13-atoms nanoclusters, from -1.53 (Co_{33}) to -1.66 eV ($\text{Ni}_{13}\text{@Co}_{20}$) and to -1.66 eV ($\text{Co@Ni}_{12}\text{@Co}_{20}$) for 33-atoms nanoclusters, and from -1.52 (Co_{55}) to -1.56 eV ($\text{Ni}_{13}\text{@Co}_{42}$) and to -1.57 eV ($\text{Co@Ni}_{12}\text{@Co}_{42}$) for 55-atoms nanoclusters. Similarly, the shift of the Co@Ni bimetallic nanoclusters with the Ni surface shell, as shown in Figures 4(i)–4(p). Quantitatively, the d-band centers are -1.25 (Ni_{13}), -1.29 (Co@Ni_{12}) eV for 13-atom particles, -1.41 (Ni_{33}), -1.50 ($\text{Co}_{13}\text{@Ni}_{20}$), -1.52 ($\text{Ni@Co}_{12}\text{@Ni}_{20}$) eV for 33-atom systems and -1.40 (Ni_{55}), -1.38 ($\text{Co}_{13}\text{@Ni}_{42}$), -1.40 ($\text{Ni@Co}_{12}\text{@Ni}_{42}$) eV for 55-atoms nanoclusters. Generally, a shallower d-band center of transition metals corresponds to higher chemical activity.¹⁷ These results show that the d-band centers of the Ni-surface nanoclusters are closer to the Fermi energy than Co-surface, indicating that the monometallic and bimetallic Co-Ni core-shell nanoclusters with Ni-surface have higher chemical activity than Co-surface.

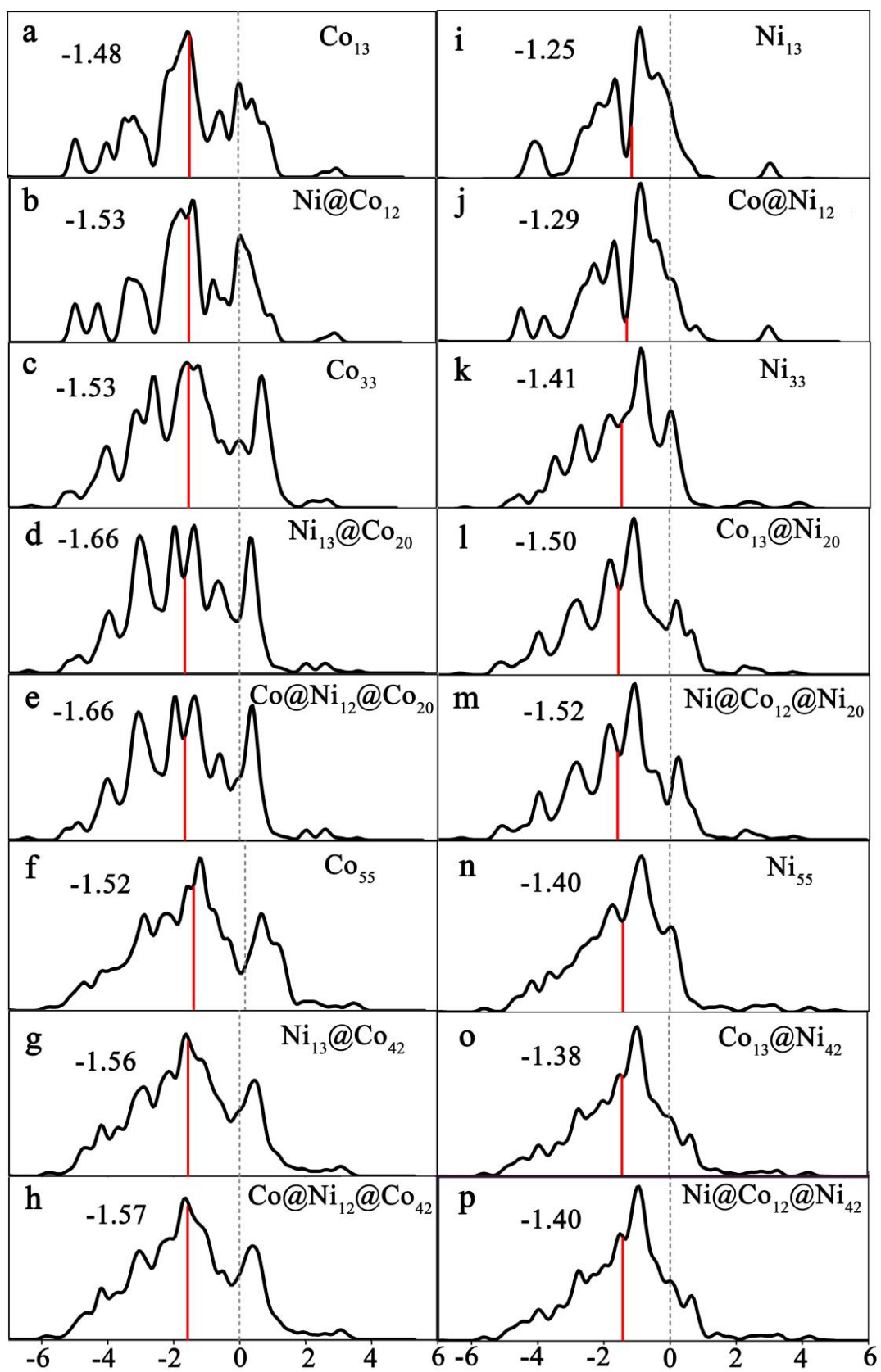


Figure 4. The densities of states projected onto the d-band of the monometallic and bimetallic Co-Ni core-shell nanoclusters. The red lines indicate the corresponding d-

band center (eV). The Fermi level is set to zero energy and indicated by the vertical dashed lines.

Co-Ni nanoclusters have good magnetic properties and complex electronic structures

To further understand these nanoclusters' electronic and magnetic properties, a partial density of states (PDOS) projected onto the core, inner-shell, and surface-shell atoms are displayed in Figures 5, 6, and 7 for the 13-, 33- and 55-atoms nanoclusters, respectively. The total magnetic moments of these nanoclusters are listed in the fourth column of Table 1. The results show that all 13-atoms nanoclusters of the Co_{13} , Ni_{13} , Ni@Co_{12} , and Co@Ni_{12} are metallic and ferromagnetic with asymmetry PDOS curves for the core and surface atoms. The monometallic and bimetallic nanoclusters with the Co-rich surface-shell of Co_{13} , Ni@Co_{12} display a higher total magnetic moment than Ni_{13} , Co@Ni_{12} with the Ni-rich surface-shell. In detail, the total magnetic moments of these nanoclusters follow the order Co_{13} ($21.77 \mu_B$) > Ni@Co_{12} ($20.64 \mu_B$) > Co@Ni_{12} ($9.05 \mu_B$) > Ni_{13} ($8.00 \mu_B$).

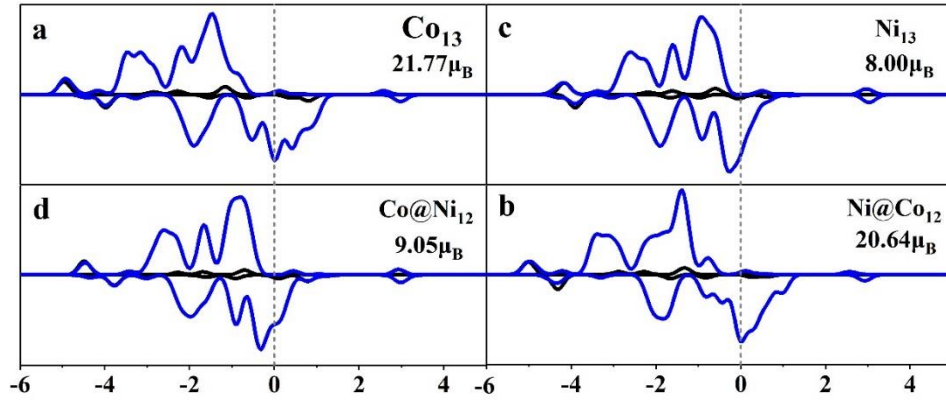


Figure 5. Partial densities of states (PDOS) are projected onto the core atom (black lines) and surface atom (blue lines) for the 13-atoms nanoclusters. The Fermi level is set to zero energy and indicated by the vertical dashed lines.

With the partial density of states (PDOS) analysis on dodecahedral 33-atoms monometallic and bimetallic nanoclusters, we found that all the atoms are metallic and ferromagnetic with asymmetry PDOS curves amount the majority and minority spins projected onto the core, middle- and surface-shell atoms (Figure 6). The Co_{33} has the

largest total magnetic moment of $60.89 \mu_B$, while the total magnetic moments of two-shell $\text{Ni}_{13}@\text{Co}_{20}$ and three-shell $\text{Co}@\text{Ni}_{12}@\text{Co}_{20}$ are 51.77 and $51.23 \mu_B$, lower than that of Co_{33} by 9.12 and $9.66 \mu_B$, respectively. The total magnetic moment of two-shell $\text{Ni}_{13}@\text{Co}_{20}$ and three-shell $\text{Co}@\text{Ni}_{12}@\text{Co}_{20}$ are weakened significantly in sequence because the core and inner shell Co atoms in Co_{33} are substituted successively by the Ni atoms. Interestingly, two-shell $\text{Co}_{13}@\text{Ni}_{20}$ has the highest total magnetic moment of $40.69 \mu_B$ in the nanoparticles with a Ni surface, higher than that of the Ni_{33} by $12.35 \mu_B$ due to the Co-substitution of the middle-shell 12 Ni atoms in Ni_{33} . While the Ni_{33} has the lowest total magnetic moment of $28.34 \mu_B$, and the three-shell $\text{Ni}@\text{Co}_{12}@\text{Ni}_{20}$ is $39.69 \mu_B$, lower than that of the Ni_{33} by $11.35 \mu_B$. The total magnetic moment of 33-atoms monometallic and bimetallic nanoclusters follows the sequence: Co_{33} ($60.89 \mu_B$) > $\text{Co}_{13}@\text{Ni}_{20}$ ($51.77 \mu_B$) > $\text{Co}@\text{Ni}_{12}@\text{Co}_{20}$ ($51.23 \mu_B$) and $\text{Co}_{13}@\text{Ni}_{20}$ ($40.69 \mu_B$) > $\text{Ni}@\text{Co}_{12}@\text{Ni}_{20}$ ($39.69 \mu_B$) > Ni_{33} ($28.34 \mu_B$).

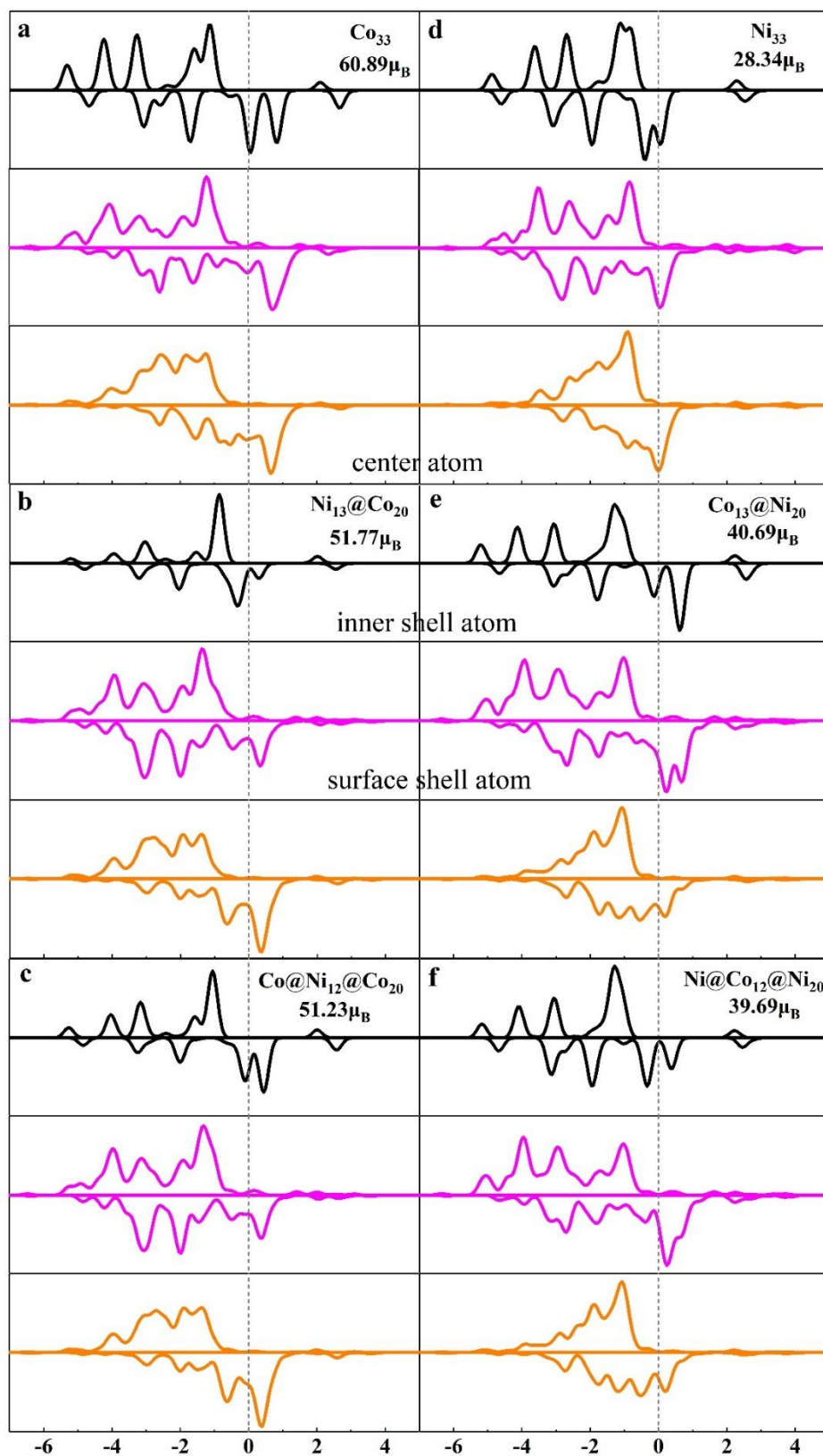


Figure 6. Partial densities of states (PDOSs) projected onto the core (black lines), inner-shell (magenta lines), surface atom (orange lines) for the 33-atoms nanoclusters. The Fermi level is set to zero energy and indicated by the vertical dashed lines.

As displayed in Figure 7. for the icosahedral 55-atoms monometallic and bimetallic nanoclusters, the Co_{55} has the largest total magnetic moment of $104.45 \mu_B$, while total magnetic moments of two-shell $\text{Ni}_{13}@\text{Co}_{42}$ and three-shell $\text{Co}@\text{Ni}_{12}@\text{Co}_{42}$ are 88.51 and $91.26 \mu_B$, lower than that of Co_{55} by 15.94 and $13.19 \mu_B$, respectively.

The total magnetic moment of three-shell $\text{Co}@\text{Ni}_{12}@\text{Co}_{42}$ and two-shell $\text{Ni}_{13}@\text{Co}_{42}$ is weakened in sequence because the core and inner shell Co atoms in the Co_{55} are substituted successively by the Ni atoms. In contrast, the Ni_{55} has the lowest total magnetic moment of $38.89 \mu_B$, while the total magnetic moment of two-shell $\text{Co}_{13}@\text{Ni}_{42}$ and $\text{Ni}@\text{Co}_{12}@\text{Ni}_{42}$ are 52.43 and $51.62 \mu_B$, higher than that of Ni_{55} by 13.54 and $12.73 \mu_B$, respectively. The total magnetic moment of two-shell $\text{Co}_{13}@\text{Ni}_{42}$ and $\text{Ni}@\text{Co}_{12}@\text{Ni}_{42}$ nanoclusters is enhanced in sequence because the core and inner shell Ni atoms in the Ni_{55} are substituted successively by the Co atoms. In one word, the total magnetic moment follows the order: Co_{55} ($104.45 \mu_B$) > $\text{Co}@\text{Ni}_{12}@\text{Co}_{42}$ ($91.26 \mu_B$) > $\text{Ni}_{13}@\text{Co}_{42}$ ($88.51 \mu_B$) and $\text{Co}_{13}@\text{Ni}_{42}$ ($52.43 \mu_B$) > $\text{Ni}@\text{Co}_{12}@\text{Ni}_{42}$ ($51.62 \mu_B$) > Ni_{55} ($38.89 \mu_B$).

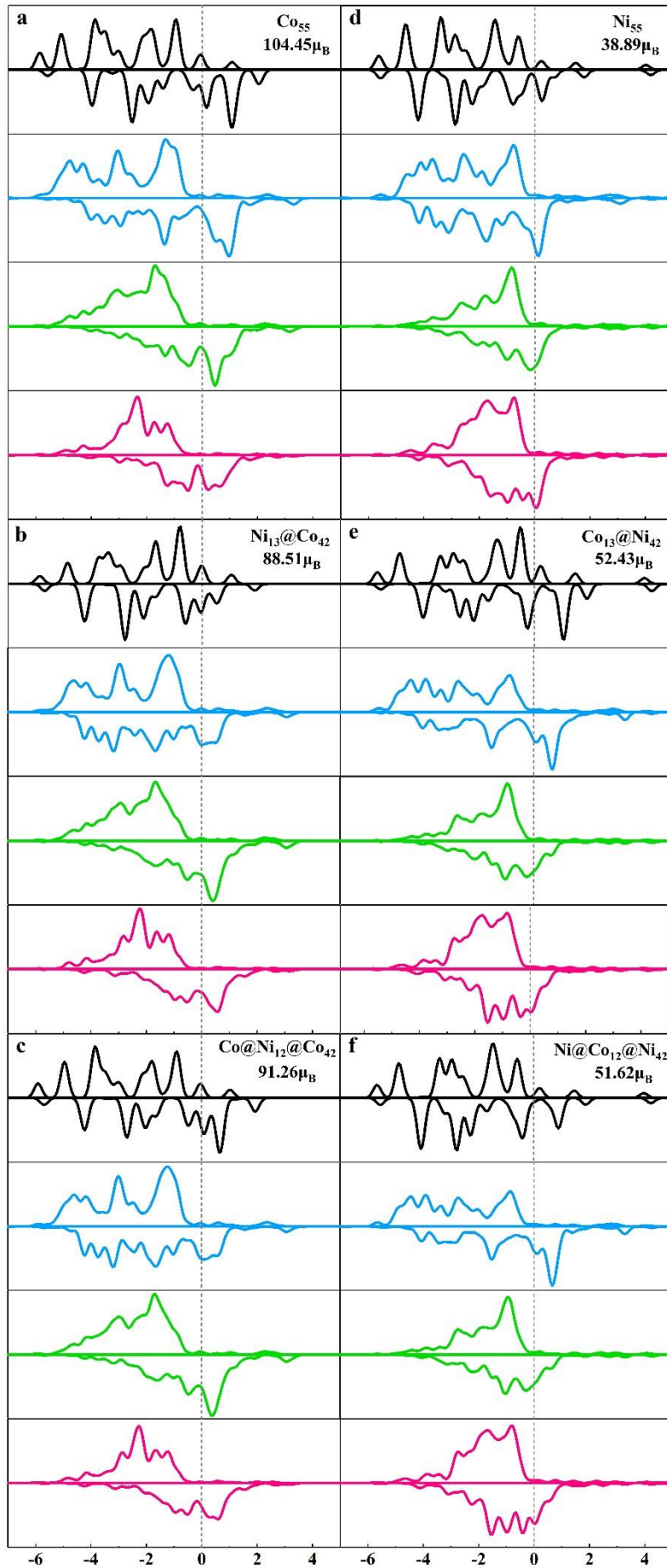


Figure 7. Partial densities of states (PDOSs) projected onto the core (black lines), inner-shell (blue lines), surface edge atom (green lines), and surface vertex (red lines) atom for the 55-atom nanoclusters. The Fermi level is set to zero energy and indicated by the vertical dashed lines.

By adjusting the size and electronic structures, Co@Ni₁₂ shows the best HER performance

The electrocatalytic activity of Co-Ni nanoclusters in Hydrogen Evolution Reaction (HER) has been intensely scrutinized for over 20 years¹⁸. Recently, the experimental findings indicated that the Co-Ni nanoclusters exhibited excellent electrocatalytic activity toward the HER.^{6, 19, 20} In order to better understand the catalytic activity difference of the Co-Ni monometallic and bimetallic nanoclusters in HER, we have further calculated the adsorption of hydrogen.

The generally accepted mechanism of the Hydrogen Evolution Reaction (HER) is that an initial state ($H^+ + e^-$), an intermediate state (adsorbed H, H^*), and a product state ($1/2H_2$) existed in an HER pathway. In addition, the reactor rate of the overall HER is directly determined by the hydrogen adsorption free energy (ΔG_{H^*}).^{21, 22} Thus, ΔG_{H^*} has been successfully employed as a good indicator for correlating theoretical predictions with experimental measurements of HER catalytic activities.²³ The optimum value of ΔG_{H^*} should be zero, implying that hydrogen adsorbent to the surface neither too weakly nor too strongly²⁴. The absolute value of free energy of hydrogen adsorption $|\Delta G_{H^*}| < 0.1\text{eV}$ can be defined as the optimal active sites⁷, demonstrated superior HER performance. The ΔG_{H^*} is expressed as follows²⁵:

$$\Delta G_{H^*} = \Delta E_{H^*} + \Delta E_{ZPE} - T\Delta S_{H^*}$$

where ΔG_{H^*} , ΔE_{ZPE} , and $T\Delta S_{H^*}$ are the chemisorption energy of atomic hydrogen on the given surface, zero-point energy difference between the adsorbed and the gas phase, and the entropy change of H^* adsorption. The zero-point energy correction can be estimated by the equation:

$$\Delta E_{ZPE} = E_{ZPE}(H^*) - \frac{1}{2}E_{ZPE}(H_2)$$

where $E_{ZPE}(H^*)$ and $E_{ZPE}(H_2)$ are calculated by vibration frequency calculation. In fact, the vibrational entropy in the adsorbed state is small, which means that the entropy of adsorption of $\frac{1}{2}H_2$ is $\Delta S_{H^*} \cong -\frac{1}{2}S_{H_2}^0$, where $S_{H_2}^0$ is the entropy of H_2 in the gas phase at standard conditions. Therefore, the value of $T\Delta S_{H^*} = -\frac{1}{2}TS_{H_2}^0 = -0.20$ eV^{26, 27}. The value of ΔE_{H^*} is calculated as:

$$\Delta E_{H^*} = E_{tot} - E_{sub} - \frac{1}{2}E_{H_2}$$

where E_{tot} and E_{sub} are the energies of H adsorbed systems and the clean given clusters, respectively, and E_{H_2} is the energy of molecular H_2 in the gas phase.

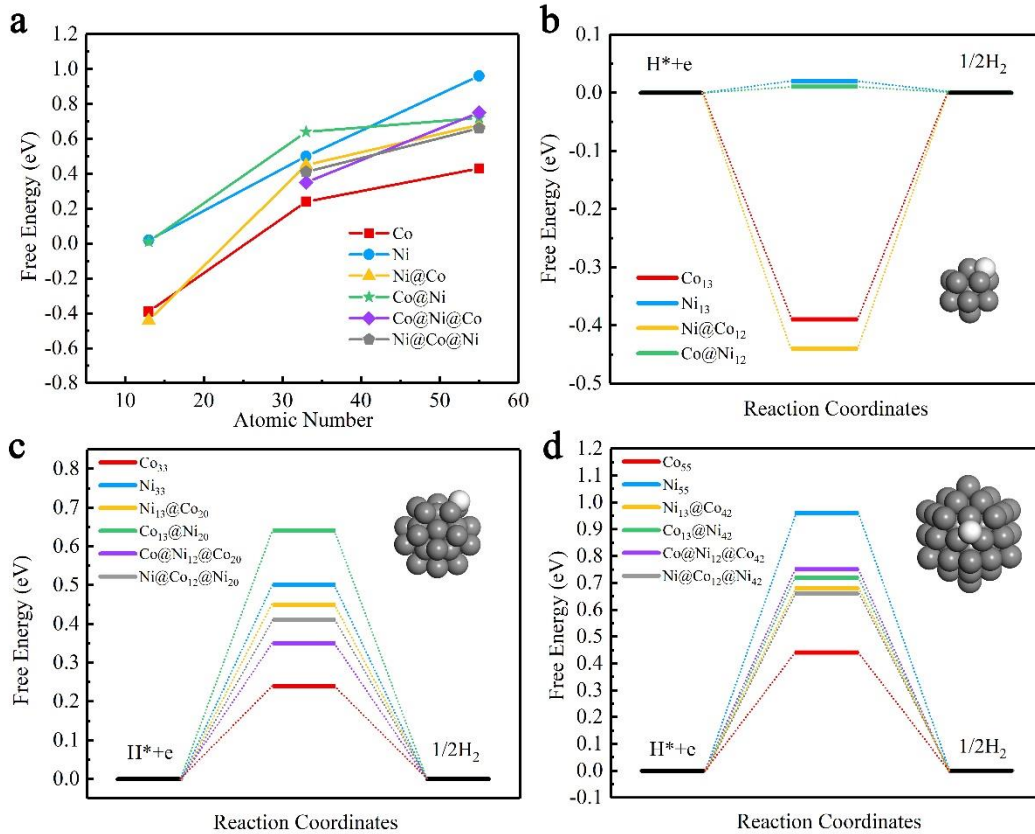


Figure 8. Calculated Gibbs free-energy diagram for HER on monometallic and bimetallic Co-Ni core-shell nanoclusters.

Figure 8 shows the calculated free energy diagram for hydrogen adsorption on 13-, 33-, and 55-atoms monometallic and bimetallic Co-Ni core-shell nanoclusters. In 13-atoms nanoclusters (Figure 8b), the absolute value of free energy of hydrogen adsorption $|\Delta G_{H^*}|$ follows the order: Co@Ni₁₂ (0.01eV) < Ni₁₃ (0.02eV) < Co₁₃ (-0.39eV) < Ni@Co₁₂ (-0.44eV). This also represents the performance order of HER is Co@Ni₁₂ (0.01eV) > Ni₁₃ (0.02eV) > Co₁₃ (0.39eV) > Ni@Co₁₂ (0.44eV). In Figure 8c, we can intuitively know that the HER performance of the 33-atoms nanoclusters from high to low is Co₃₃ (0.24eV) > Co@Ni₁₂@Co₂₀ (0.35eV) > Ni@Co₁₂@Ni₂₀ (0.41eV) > Ni₁₃@Co₄₂ (0.45eV) > Ni₃₃ (0.50eV) > Co₁₃@Ni₂₀ (0.64eV). Similarly, HER performance of the 55-atoms nanoclusters from high to low is Co₅₅ (0.44eV) > Ni@Co₁₂@Ni₄₂ (0.66eV) > Ni₁₃@Co₄₂ (0.68eV) > Co₁₃@Ni₄₂ (0.72eV) > Co@Ni₁₂@Co₄₂ (0.75eV) > Ni₅₅ (0.96eV). Detailed HER analysis data can be found in the supporting information Table S4.

In general, the calculation and analysis of HER performance indicate that Co@Ni₁₂ ($|\Delta G_{H^*}|=0.01\text{eV}$) shows the best HER performance. In addition, in Figure 8a, we can understand that the Gibbs free energy of hydrogen adsorption ΔG_{H^*} of Co-Ni nanoclusters is positively related to the size of the clusters, and the ΔG_{H^*} can be adjusted within a certain range by changing the electronic structure of the clusters.

CONCLUSIONS

In conclusion, the geometrical structure, thermodynamic stability, chemical activity, electronic and magnetic properties, and catalytic activity in HER of the 13- 33- and 55-atoms monometallic and bimetallic Co-Ni core-shell nanoclusters were systematically studied using DFT calculations. Through structure analysis, We know the Co-Ni Core-shell alloyed clusters show similar geometries. We found that Ni-surface nanoclusters have higher relative stability than Co-surface nanoclusters by excess energy analysis. More interestingly, Ni-surface nanoclusters show higher chemical activity than Co-surface by DOS analysis using the d-band center theory. In addition, we found that Co-Ni nanoclusters have good magnetic properties and complex electronic structures. To

further understand the catalytic properties of these nanoclusters, we further calculated the free energy of hydrogen adsorption and systematically studied the HER performance of Co-Ni nanoclusters. Finally, we found that the Gibbs free energy of hydrogen adsorption ΔG_{H^*} of Co-Ni nanoclusters is positively related to the size of the clusters, and the ΔG_{H^*} can be adjusted within a certain range by changing the electronic structure of the clusters. By optimizing the electronic structures and promote effective charge transfer in Co-Ni nanoclusters, a 13-atoms size bimetallic Co-Ni core-shell nanocluster Co@Ni₁₂ ($|\Delta G_{H^*}|=0.01\text{eV}$) was found to have the best HER performance.

Conflict of Interest: The authors declare that there are no conflicts of interest.

SUPPORTING INFORMATION

- See Supporting information for the optimized structure parameters of the 13- and 55-atom Co, Ni monometallic, and bimetallic Co-Ni core-shell nanoclusters (PDF).

ACKNOWLEDGMENTS

We are grateful to my personal workstation, codenamed "Hydrogen". Thanks to Tsinghua University for providing the copyright of the VASP software. Part of the work was inspired by the author (Hengyue Xu) when he visited the Tianjin Institute of Pharmaceutical Research. We also appreciate the inspiring discussions at Nanjing Tech University, especially Dr. Qiang Wang, Dr. Dengming Ming, and Dr. Pengfei Liu, who offered valuable manuscript preparation advice. Thanks to Ye Wang, a small number of pictures were made with his help.

REFERENCE

1. Xu, H.; Shang, H.; Wang, C.; Du, Y., Ultrafine Pt-based nanowires for advanced catalysis. *Advanced Functional Materials* **2020**, *30* (28), 2000793.
2. Xu, H.; Shang, H.; Wang, C.; Du, Y., Low-Dimensional Metallic Nanomaterials for Advanced Electrocatalysis. *Advanced Functional Materials* **2020**, *30* (50), 2006317.
3. Wang, J.; Shao, H.; Ren, S.; Hu, A.; Li, M., Fabrication of porous Ni-Co catalytic electrode with high performance in hydrogen evolution reaction. *Applied Surface Science* **2021**, 539.

4. Li, S.; Wang, Y.; Peng, S.; Zhang, L.; Al-Enizi, A. M.; Zhang, H.; Sun, X.; Zheng, G., Co-Ni-Based Nanotubes/Nanosheets as Efficient Water Splitting Electrocatalysts. *Advanced Energy Materials* **2016**, *6* (3).
5. Li, Y.; Zhang, X.; Hu, A.; Li, M., Morphological variation of electrodeposited nanostructured Ni-Co alloy electrodes and their property for hydrogen evolution reaction. *International Journal of Hydrogen Energy* **2018**, *43* (49), 22012-22020.
6. Darband, G. B.; Aliofkhaeizaei, M.; Rouhaghdam, A. S.; Kiani, M., Three-dimensional Ni-Co alloy hierarchical nanostructure as efficient non-noble-metal electrocatalyst for hydrogen evolution reaction. *Applied Surface Science* **2019**, *465*, 846-862.
7. Mao, X.; Wang, L.; Xu, Y.; Wang, P.; Li, Y.; Zhao, J., Computational high-throughput screening of alloy nanoclusters for electrocatalytic hydrogen evolution. *npj Computational Materials* **2021**, *7* (1).
8. Kresse, G.; Furthmüller, J., Efficiency of ab-initio total energy calculations for metals and semiconductors using a plane-wave basis set. *Computational materials science* **1996**, *6* (1), 15-50.
9. Perdew, J. P.; Burke, K.; Ernzerhof, M., Generalized gradient approximation made simple. *Physical review letters* **1996**, *77* (18), 3865.
10. Kresse, G.; Joubert, D., From ultrasoft pseudopotentials to the projector augmented-wave method. *Physical Review B* **1999**, *59* (3), 1758.
11. Blöchl, P. E., Projector augmented-wave method. *Physical review B* **1994**, *50* (24), 17953.
12. Silaghi, M.-C.; Comas-Vives, A.; Copéret, C., CO₂ Activation on Ni/ γ -Al₂O₃ Catalysts by First-Principles Calculations: From Ideal Surfaces to Supported Nanoparticles. *ACS Catalysis* **2016**, *6* (7), 4501-4505.
13. Sanville, E.; Kenny, S. D.; Smith, R.; Henkelman, G., Improved grid-based algorithm for Bader charge allocation. *Journal of computational chemistry* **2007**, *28* (5), 899-908.
14. Henkelman, G.; Arnaldsson, A.; Jónsson, H., A fast and robust algorithm for Bader decomposition of charge density. *Computational Materials Science* **2006**, *36* (3), 354-360.
15. Ferrando, R.; Jellinek, J.; Johnston, R. L., Nanoalloys: from theory to applications of alloy clusters and nanoparticles. *Chemical reviews* **2008**, *108* (3), 845-910.
16. Piotrowski, M. J.; Piquini, P.; Da Silva, J. L., Platinum-Based Nanoalloys Pt_nTM_{55-n} (TM= Co, Rh, Au): A Density Functional Theory Investigation. *The Journal of Physical Chemistry C* **2012**, *116* (34), 18432-18439.
17. Hammer, B.; Nørskov, J., Impact of Surface Science on Catalysis ed BC Gates and H Knözinger. London: Academic) p: 2000.
18. Correia, A. N.; Machado, S. A.; Avaca, L. A., Studies of the hydrogen evolution reaction on smooth Co and electrodeposited Ni-Co ultramicroelectrodes. *Electrochemistry communications* **1999**, *1* (12), 600-604.
19. González-Buch, C.; Herraiz-Cardona, I.; Ortega, E.; García-Antón, J.;

Pérez-Herranz, V., Synthesis and characterization of macroporous Ni, Co and Ni–Co electrocatalytic deposits for hydrogen evolution reaction in alkaline media. *International journal of hydrogen energy* **2013**, *38* (25), 10157-10169.

20. Lupi, C.; Dell'Era, A.; Pasquali, M., Nickel–cobalt electrodeposited alloys for hydrogen evolution in alkaline media. *international journal of hydrogen energy* **2009**, *34* (5), 2101-2106.

21. Benck, J. D.; Hellstern, T. R.; Kibsgaard, J.; Chakthranont, P.; Jaramillo, T. F., Catalyzing the Hydrogen Evolution Reaction (HER) with Molybdenum Sulfide Nanomaterials. *ACS Catalysis* **2014**, *4* (11), 3957-3971.

22. Jiao, Y.; Zheng, Y.; Jaroniec, M. T.; Qiao, S. Z., Design of electrocatalysts for oxygen- and hydrogen-involving energy conversion reactions. *Chem. Soc. Rev.* **2015**, *44* (8), 2060-2086.

23. Tang, Y.-J.; Wang, Y.; Wang, X.-L.; Li, S.-L.; Huang, W.; Dong, L.-Z.; Liu, C.-H.; Li, Y.-F.; Lan, Y.-Q., Molybdenum Disulfide/Nitrogen-Doped Reduced Graphene Oxide Nanocomposite with Enlarged Interlayer Spacing for Electrocatalytic Hydrogen Evolution. *Advanced Energy Materials* **2016**, *6* (12).

24. Seh, Z. W.; Kibsgaard, J.; Dickens, C. F.; Chorkendorff, I. B.; Norskov, J. K.; Jaramillo, T. F., Combining theory and experiment in electrocatalysis: Insights into materials design. *Science* **2017**, *355* (6321), 146-+.

25. Yang, Y.; Lun, Z. Y.; Xia, G. L.; Zheng, F. C.; He, M. N.; Chen, Q. W., Non-precious alloy encapsulated in nitrogen-doped graphene layers derived from MOFs as an active and durable hydrogen evolution reaction catalyst. *Energy Environ. Sci.* **2015**, *8* (12), 3563-3571.

26. Nørskov, J. K.; Bligaard, T.; Logadottir, A.; Kitchin, J.; Chen, J. G.; Pandelov, S.; Stimming, U., Trends in the exchange current for hydrogen evolution. *Journal of The Electrochemical Society* **2005**, *152* (3), J23.

27. Wang, Q.; Lu, X.; Zhen, Y.; Li, W.-q.; Chen, G.-h.; Yang, Y., Structure, stability, electronic, magnetic, and catalytic properties of monometallic Pd, Au, and bimetallic Pd–Au core-shell nanoparticles. *The Journal of chemical physics* **2018**, *149* (24), 244307.